SICE Annual Conference 2010
August 18-21, 2010, The Grand Hotel, Taipei, Taiwan

High Accuracy Analysis Method for 3D Nanoscale Deformation / Fracture Characteristics inside a Material

Mitsuru Nakazawa*, Masakazu Kobayashi†, Hiroyuki Toda† and Yoshimitsu Aoki‡
{*Graduate School, ‡Faculty} of Science and Technology, Keio University
3-14-1, Hiyoshi, Kohoku-ku,Yokohama, Kanagawa, 223-8522, JPN, Email: mnakazawa@aoki-medialab.org, aoki@elec.keio.ac.jp
†Department of Production Systems Engineering, Toyohashi University of Technology
1-1, Hibarigaoka, Tempakucho, Toyohashishi, Aichi 441-8580, JPN, Email: {m-kobayashi,toda}@pse.tut.ac.jp

***Abstract*—To evaluate internal thorough material characteristics in deformation, we proposed an analysis method which obtains displacement vectors of dispersed particles between deformation from nano-order 3D-CT images. In this paper, we introduce an improved approach to achieve more robust matching and eliminate the need to tune some parameters. To confirm the effectiveness of the improved approach, virtual tensile tests are carried out. Precision is achieved more than 99% at every matching between adjacent load steps.**

***Keywords*—material evaluation; nano-order observation; 3D-CT; PTV**

I. Introduction

In material engineering, it is widely recognized that Deformation / Fracture (D/F) characteristics are important because these characteristics prove the safety of developed materials. D/F characteristics are analyzed by the load required to break the material, and the deformation caused by the load. Traditional methods, which include the grid method [1], [2], the strain gage method [3], [4], [5] and the optical (Moiré) method [6], [7], [8], are restricted to surface strain. However, as shown in Fig.I, micro-scale internal structures such as bubbles (pores), dispersed particles and cracks are contained in the material. Actually, more than ten thousand of them in $1\mathrm{mm}^3$ affect D/F characteristics. These structures are critical to the functionality of bumper materials for absorbing accidental shocks, or turbine materials of nuclear power plants. Moreover, the D/F characteristics on the surface do not relate to those on the inside. Therefore, it is required to analyze nano-scale D/F characteristics inside materials.

As non-destructive inspection, the method using X-ray and ultrasonic 3D-Computed Tomography (CT) have been quoted. Recently, SPring-8, the third generation synchrotron radiation facility, enabled to take shape 3D-CT images of materials with nano-order resolution (Figures 2 and 3) [9].

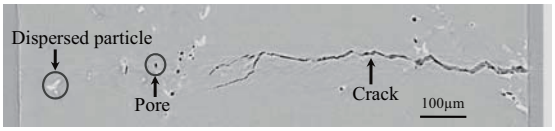

Fig. 1. Internal structures inside a material

To evaluate thorough D/F characteristics from nano-order 3D-CT images, Wert observed displacement vectors of implanted foreign particles as markers [10]. However, in terms of penetration of X-rays, the implantable markers are limited in size. Moreover, the markers have the possibility of affecting the original material characteristics.

In contrast, we have proposed an analysis method by obtaining displacement vectors of actual internal structures between deformation [11]. Fig.4 shows the flowchart of our proposed method. Internal structures are extracted from 3D-CT material images both before and after deformation. Then matching between deformation is carried out in order to obtain the displacement vectors of the internal structures. However, these vectors include the translation and the rotation of the material. Therefore, 3D strain distribution is acquired to evaluate the D/F characteristic of the material. The method for extracting internal structures and for acquiring 3D strain distribution are already constructed [11]. Hence, we focus on matching.

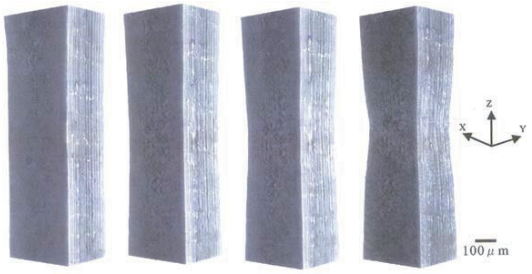

Fig. 2. 3D-CT images of a trial material

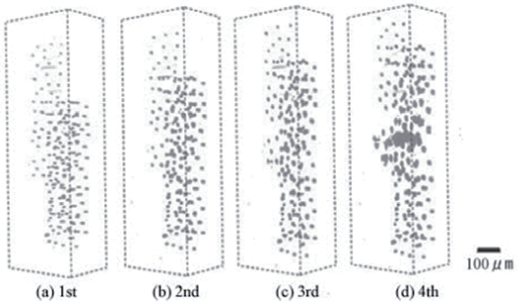

Fig. 3. Pores inside Fig.2

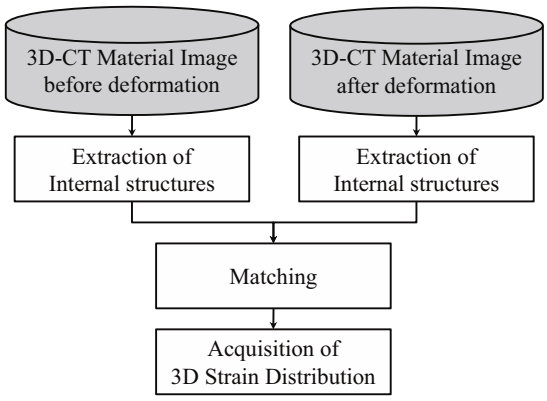

Fig. 4. Flowchart of our proposed method

Particle Image Velocimetry (PIV) obtains average displacement vectors of particles between images. PIV includes the direct cross-correlation method [16] and the FFT-based cross-correlation method [17]. However, PIV cannot apply to match internal structures because a material position is unfixed during a test. In nano-order observation, great translation and rotation occur by a little factor. Furthermore, 3D-PIV is more difficult than 2D-PIV because a cross-correlation peak weakly appears. Meanwhile, Particle Tracking Velocimetry (PTV) obtains displacement vectors of particles between images. PTV includes the method by a genetic algorithm [18] and by a neural network [19]. However it is difficult to match more than ten thousand internal structures because of long processing time and complex parameter tuning.

In actual materials, dispersed particles are deformation-proof and may be various in form. Additionally, their displacement must obey material mechanics. Therefore, to match more than ten thousand dispersed particles, we have suggested a stratified matching approach. Dispersed particles larger than a volume threshold $V_{\rm th}$ voxels were classified as landmarks. The others were non-landmarks. Landmarks were matched by the relaxation method [12] to obtain approximate displacement of a material. To match non-landmarks between deformation, Radial Basis Function Transform (RBFT) [13] estimated their displacement vectors based on those of landmarks. This non-landmark matching gave dense displacement distribution of a material.

In the paper [11], approximately six thousand dispersed particles were matched between simulated deformation in order to verify the stratified matching approach. Successful results proved the effectiveness of the approach. However, the approach has two problems. First, matching results depend on the volume threshold of landmarks $V_{\rm th}$. A optimal $V_{\rm th}$ needs to be given. Second, a parameter of RBFT changes the estimated displacement vectors of non-landmarks. The parameter was roughly determined by a simple search method based on the spring model [14].

To solve the above problems, we introduce an improved method in this paper. The method prepares a number of volume thresholds. Then matching by using each threshold is conducted in parallel. After that, the best matching results is adopted. The parameter of RBFT is strictly optimized by Particle Swarm Optimization (PSO) [15]. Furthermore, some techniques are added in order to achieve more robust matching.

II. Landmark Matching

Dispersed particles larger than a volume threshold $V_{\rm th}$ voxels are classified as landmarks.

A. Relaxation Method

The relaxation method [12] is employed to match landmarks between deformation. This method is under the assumption that "if a certain landmark is mismatched, its neighborhoods cannot be matched, either". Yamamoto developed this method to apply to recognize handprinted Kanji characters [20]. The method was also used for velocity field estimation on sea surface [21], facial parts detection [22] and content-based image retrieval [23].

Here, the number of landmarks before and after deformation are N and M. The set of landmarks before and after deformation are expressed as $A = \{a_1, a_2, \cdots, a_N\}$ and $B = \{b_1, b_2, \cdots, b_M\}$, respectively. Then a probability vector between a_i and B is expressed as $\boldsymbol{p_i} = \left[p_{i(1)}, \cdots, p_{i(M)}\right] \in R^M$. Probability is always positive and satisfies $\sum_{k'} p_{i(k')} = 1$. The set of N probability vectors constitutes a probability matrix between A and B $\boldsymbol{p} = [\boldsymbol{p_1}, \cdots, \boldsymbol{p_N}]^{\rm T} \in R^{N \times M}$.

1) Initialization of the Probability Matrix: If a volume change between a_i and b_k is markedly great, then $p_{i(k)}$ should be zero; otherwise, it is given the same probability as the others (Eq.1).

$$p^{0'}_{i(k)} = \begin{cases} 1 & \text{if } \left|\frac{V_k - V_i}{V_i}\right| \le \mathrm{RC} \\ 0 & \text{otherwise} \end{cases},$$

$$p^{0}_{i(k)} = \frac{p^{0'}_{i(k)}}{\sum_{k'} p^{0'}_{i(k')}}, \tag{1}$$

where V_i and V_k are the volume of a_i and of b_k respectively. Additionally, we define an allowable volume change RC in order to ignore the matching relations which are markedly-great volume changes.

2) Renewal of the Probability Matrix: $p_{i(k)}$ is renewed by a renewal coefficient $q_{i(k)}$ as shown in Eq.2.

$$p^{t+1}_{i(k)} = \frac{q_{i(k)} p^{t}_{i(k)}}{\sum_{k'} q_{i(k')} p^{t}_{i(k')}}, \tag{2}$$

$$q_{i(k)} = \sum_{j \in \zeta_i} \max_{l} \left(\gamma_{ij}\left(k,\ l\right) p^{t}_{j(l)}\right), \tag{3}$$

$$\gamma_{ij}\left(k,\ l\right) = \max\left(1 - \frac{1}{\mathrm{W}} e_{ij}\left(k,\ l\right),\ 0\right), \tag{4}$$

$$e_{ij}\left(k,\ l\right) = \frac{\|\boldsymbol{d_{kl}} - \boldsymbol{d_{ij}}\|}{\|\boldsymbol{d_{ij}}\|}. \tag{5}$$

$q_{i(k)}$ represents the conformity with the neighborhood set of a_i, provided that a_i matches b_k. To define the neighborhood

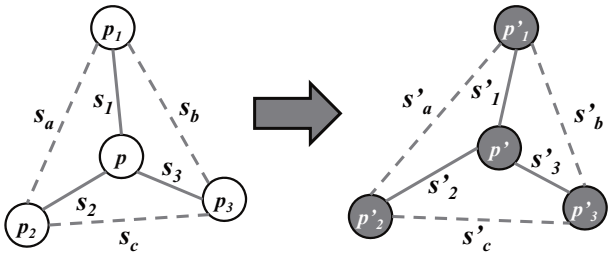

$\boldsymbol{s_1}$: Spring vector from a landmark to the neighborhoods
$\boldsymbol{s_a}$: Spring vector between the neighborhoods

Fig. 5. Spring model

set ζ_i, Qhull[24] constructs undirected graphs G by generating Delaunay tetrahedrons from A. Then, let ζ_i denote $\{a_{j'} \mid [a_i,\ a_{j'}] \in G,\ i \neq j'\}$. To find the likeliest-matching candidate b_l of a neighborhood a_j, the product of $\gamma_{ij}\,(k,\ l)$ and the present probability $p^t_{j(l)}$ is calculated for each landmark after deformation. The landmark after deformation which has the maximum product is regard as the candidate b_l.

As shown in Eq.3, $q_{i(k)}$ is obtained by summing the above maximum product of each neighborhood. Here, $\gamma_{ij}\,(k,\ l)$ is the evaluation function of matching $a_i \leftrightarrow b_k$ and $a_j \leftrightarrow b_l$. This function is a decreasing function, which is calculated from the ratio of expansion and contraction $e_{ij}\,(k,\ l)$ in Eq.5. As shown in Eq.4, when $e_{ij}\,(k,\ l)$ is 0, $\gamma_{ij}\,(k,\ l)$ becomes 1 as the maximum value. On the other hand, when $e_{ij}\,(k,\ l)$ is over a ratio W which is given in advance, $\gamma_{ij}\,(k,\ l)$ becomes 0.

If the sum of the absolute differences of probability $\Delta_i = \sum_{k'} \left| p^{t+1}_{i(k')} - p^t_{i(k')} \right|$ is below a threshold δ, $\boldsymbol{p_i}$ can be considered to be converged. a_i matches the one which has the highest probability in B.

B. Deletion of Overlap Matching

When two or more landmarks before deformation match one after deformation, it is obvious that mismatching occurs in landmarks before deformation (overlap matching). When this overlap matching occurs, E_i is evaluated based on the spring model (Fig.5, Eq.6).

$$E_i = \frac{1}{N} \sum_{s \in \zeta_i} \frac{\|\boldsymbol{d'_{is}} - \boldsymbol{d_{is}}\|}{\|\boldsymbol{d_{is}}\|} + \frac{1}{M} \sum_{s,t \in \zeta_i, s \neq t} \frac{\|\boldsymbol{d'_{st}} - \boldsymbol{d_{st}}\|}{\|\boldsymbol{d_{st}}\|}, \tag{6}$$

where N is the total number of the neighborhoods. M is the number of 2-combinations from the neighborhoods, namely $M = {}_N\mathrm{C}_2$. E_i consists of the sum of two average ratios of expansion and contraction. The left term of Eq.6 is that from a landmark to its neighborhoods and the right one is that between the neighborhoods.

The landmark before deformation which has the minimum E_i matches the one after deformation. The others are rejected.

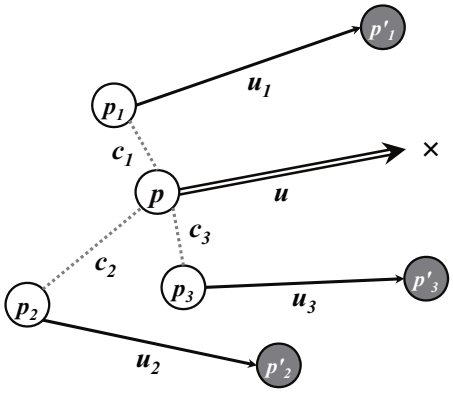

$\boldsymbol{p}$: Position vector of a non-landmark before deformation
$\boldsymbol{p_i}$: Position vector of a landmark before deformation
$\boldsymbol{p'_i}$: Position vector of a landmark after deformation
$\boldsymbol{u}$: Estimated displacement vector of a non-landmark
$\boldsymbol{u_i}$: Displacement vector of a landmark
$\boldsymbol{c_i}$: Weighting coefficient

Fig. 6. Radial Basis Function Transform

III. Non-landmark Matching

The displacement vectors of non-landmarks are estimated by those of landmarks.

A. Vector Estimation by RBFT and Matching

In order to estimate 3D displacement vectors, Radial Basis Function Transform (RBFT) [13] is employed. A radial basis function (RBF) is a monotonically decreasing function as shown in Eq.7.

$$g(r) = \exp(-kr), \tag{7}$$

where k is a parameter to adjust the RBF. The RBF is used to weight interpolation coefficients corresponding to distances between a non-landmark and landmarks. The principle of the RBFT is explained as follows.

First, an interpolation coefficient $\boldsymbol{c} = \{\boldsymbol{c_1}, \cdots, \boldsymbol{c_N}\}$ can be calculated as Eq.8 because both the displacement vectors of landmarks and the distances between landmarks before deformation are already known.

$$\boldsymbol{u_i} = \sum_{j=1}^{N} \boldsymbol{c_j}\, g(\|\boldsymbol{p_i} - \boldsymbol{p_j}\|), \tag{8}$$

where N is the number of landmarks. Note that the interpolation coefficient of a landmark $\boldsymbol{c_j}$ has three components along the x-, y- and z-axes.

The matrix representation of Eq.8 is given in Eq.9. As shown in Eq.10, we multiply both sides of Eq.9 by the inverse of the RBF matrix to obtain the interpolation coefficient matrix.

$$\begin{pmatrix} u_{x1} \dots u_{xN} \\ u_{y1} \dots u_{yN} \\ u_{z1} \dots u_{zN} \end{pmatrix} = \begin{pmatrix} c_{x1} \dots c_{xN} \\ c_{y1} \dots c_{yN} \\ c_{z1} \dots c_{zN} \end{pmatrix} \begin{pmatrix} g(\|\boldsymbol{p_1} - \boldsymbol{p_1}\|) & \dots & g(\|\boldsymbol{p_N} - \boldsymbol{p_1}\|) \\ \vdots & \ddots & \vdots \\ g(\|\boldsymbol{p_1} - \boldsymbol{p_N}\|) & \dots & g(\|\boldsymbol{p_N} - \boldsymbol{p_N}\|) \end{pmatrix}. \tag{9}$$

$$\begin{pmatrix} c_{x1} \dots c_{xN} \\ c_{y1} \dots c_{yN} \\ c_{z1} \dots c_{zN} \end{pmatrix} = \begin{pmatrix} u_{x1} \dots u_{xN} \\ u_{y1} \dots u_{yN} \\ u_{z1} \dots u_{zN} \end{pmatrix} \begin{pmatrix} g(\|\boldsymbol{p_1} - \boldsymbol{p_1}\|) & \dots & g(\|\boldsymbol{p_N} - \boldsymbol{p_1}\|) \\ \vdots & \ddots & \vdots \\ g(\|\boldsymbol{p_1} - \boldsymbol{p_N}\|) & \dots & g(\|\boldsymbol{p_N} - \boldsymbol{p_N}\|) \end{pmatrix}^{-1}. \tag{10}$$

Then, the displacement vector of a non-landmark $\boldsymbol{u}$ can be estimated from the obtained interpolation coefficient $\boldsymbol{c}$ and the distances between the non-landmark and landmarks. The 3D vectors can be calculated by matrix operation as in Eq.12.

$$\boldsymbol{u} = \sum_{i=1}^{N} \boldsymbol{c_i} g(\|\boldsymbol{p} - \boldsymbol{p_i}\|). \tag{11}$$

$$\begin{pmatrix} u_x \\ u_y \\ u_z \end{pmatrix} = \begin{pmatrix} c_{x1} \dots c_{xN} \\ c_{y1} \dots c_{yN} \\ c_{z1} \dots c_{zN} \end{pmatrix} \begin{pmatrix} g(\|\boldsymbol{p} - \boldsymbol{p_1}\| \\ \vdots \\ g(\|\boldsymbol{p} - \boldsymbol{p_N}\|) \end{pmatrix}. \tag{12}$$

The non-landmark before deformation matches the one after deformation which is the nearest from the estimated position.

When overlap matching occurs, non-landmark before deformation which has the minimum norm between a matching and the estimated vector matches that after deformation. The others are rejected.

B. Optimal Decision of k

In Eq.7, k is the parameter to adjust a RBF. Changing k affects estimated vectors and even matching results; therefore, it is essential to determine an optimal k.

1) Restriction of the Searching Range: k is a positive value; however, it is unnecessary to search all range of k because RBFT does not work when k approaches limit values. The reason is explained as follows. When k approaches $+0$, all elements of the RBF matrix of Eq.9 are 1. The displacement vector $\boldsymbol{u}$ cannot be obtained because the inverse matrix does not exist. Meanwhile, the RBF matrix of Eq.12 as k approaches $+\infty$ is $\mathbf{0}$. It is obvious that the displacement vector $\boldsymbol{u}$ is $\mathbf{0}$.

In our study, k is restricted by using the RBF matrix of Eq.9. The range of k is determined to satisfy that all off-diagonal elements of the RBF matrix are neither 1 nor 0.

2) Optimal Decision by PSO: Particle Swarm Optimization (PSO) [15] is an optimization method based on the idea of swarm intelligence. PSO consists of some individuals (candidate solutions), each of which has its position and velocity. The individuals search an optimal position while sharing information with the others. The position of each individual is evaluated by a fitness function. PSO has advantages of fewer parameters than other methods and robust solution searching for continuous values. The procedure of PSO is described as follows.

First, individuals are randomly set in a search space. Then, as shown in Eq.13 and Eq.14, the position $\boldsymbol{x}_i$ and the velocity $\boldsymbol{v}_i$ of each individual are renewed by its own best position ever (local best: $\boldsymbol{l}_i$) and the best position in all individuals (global best: $\boldsymbol{g}$).

$$\boldsymbol{x}_i(t+1) = \boldsymbol{x}_i(t) + \boldsymbol{v}_i(t+1), \tag{13}$$

$$\boldsymbol{v}_i(t+1) = \omega \boldsymbol{v}_i(t) + C_1 \lambda_1 (\boldsymbol{l}_i - \boldsymbol{x}_i(t)) + C_2 \lambda_2 (\boldsymbol{g} - \boldsymbol{x}_i(t)), \tag{14}$$

where ω named "inertia" is set to a value near 1. C_1 and C_2 are weighting coefficient for the local and the global bests respectively. Both coefficient are set to 2.0. λ_1 and λ_2 are random values from 0.0 to 1.0.

To apply PSO to search the optimal k of the RBF, the fitness function of k: $f(k)$ has to be defined. Here k is expressed as the common logarithm because k is the exponential index. We define $f(k)$ as the sum of norms between the matching and the estimated vectors of each dispersed particle. To determine an optimal k, PSO searches k which minimizes a function value in the restricted range.

IV. Matching Parallelization

In the previous work [11], it is already known that matching results depend on the volume threshold of landmarks V_{th}. Therefore, we prepare a number of volume thresholds. Then each matching by using each volume threshold is performed in parallel. In addition, mismatch landmarks negatively affected non-landmark estimation. Therefore, the estimation is iterated while a percentage of landmarks is randomly selected.

Matching results are evaluated by using the spring model described in Subsection II-B. The displacement vectors of rejected dispersed particles before deformation are estimated by RBFT as if the particles were at the estimated position in the material after deformation (Fig.8).

The best matching result is adopted by evaluating how small average ratios of expansion and contraction are.

V. Experiments

A. Experimental Outline

In actual tests, our proposed method cannot be evaluated because it is almost impossible to obtain the correct matching answer between deformation due to too many numbers of dispersed particles. Consequently, simulated tests were conducted instead of actual tests.

A model before deformation contained twenty thousand dispersed particles. The dispersed particles were randomly set. Their volumes were given based on the volumetric distribution of approximately seventeen thousand dispersed particles in an actual 2024-aluminum, the 3D-CT image of which was taken in SPring-8. Experimental environment was assumed as follows: the model size was $0.6 \times 0.6 \times 0.65\mathrm{mm}^3$, a 3D-CT image resolution was $0.5\mathrm{mm}^3/\mathrm{voxel}$ and an imaging range was $1700 \times 1700 \times 1312\mathrm{voxels}$.

We attempted to make the tests close to actual tests by considering both global and local displacement of a material. Additionally, volumetric errors in actual observation were also simulated. In this simulation, artifacts and disrupted particles were excluded because they occur in a limited situation. The details of the simulation are described as follows.

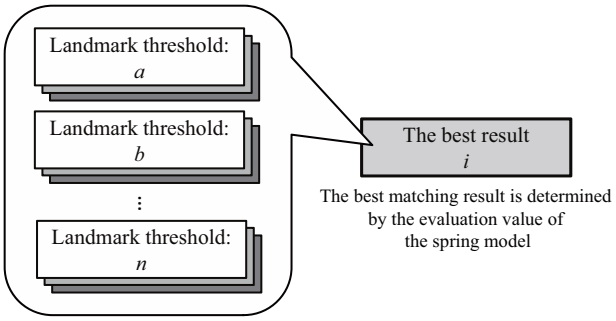

Fig. 7. Parallelization of matching procedures

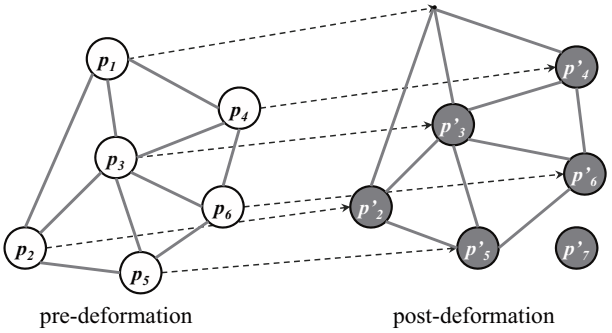

Fig. 8. Evaluation of matching results

1) Global Deformation
Plastic deformation of aluminum alloy was simulated in tensile test. The simulated model homogeneously deformed from load step 0% to 10%. After that, a necking occurred in the model like an actual aluminum. The necking geometry was given as a Gaussian curve. In a cylindrical coordinate system of r, θ and z, a strain function along the r-axis $\epsilon_r(r,\theta,z)$ is expressed as Eq.15.

$$\epsilon_r(r,\theta,z) = a\exp\left(\frac{-(z-b)^2}{2(c/3)^2}\right), \qquad (15)$$

where z corresponds to the tensile direction. Three parameters a, b and c dominate the value of $\epsilon_r(r,\theta,z)$. The parameter values of each load step are shown in Table.I.
The strain along the z-axis was calculated under the constant-volume condition with the constant strains and symmetrical condition. The parameter setting of when b=0 and c=Inf. means homogeneous deformation without a necking. The dispersed particles were changed their position by simulated material plastic flows.
2) Local Deformation
Metallic material consists of many crystal grains. The orientation of the grains affects local deformation behaviors. The rotation and the shear of the grains were considered and given by Eq.16 and Eq.17. It was assumed that these values were proportionally increased with increasing the global strain given by Eq.15.

$$\theta_{\rm rot} = \epsilon_z(r,\theta,z)\,N(0,\ C_{\rm rot}/3), \qquad (16)$$
$$\gamma_{\rm shear} = C_{\rm shear}|\epsilon_z(r,\theta,z)|, \qquad (17)$$

where N is a normal distribution. $C_{\rm rot}$ and $C_{\rm shear}$ are fitting parameters. These parameters in the present study were set as follows: $C_{\rm rot} = 5\,{\rm deg},\ C_{\rm shear} = 1$.
3) Volumetric Errors in observation
The volumes of dispersed particles are changed whenever a 3D-CT image is taken. The errors were simulated based on actual volumetric differences of dispersed particles observed in SPring-8. Here, the radius of a sphere r corresponding to a volume V is calculated by Eq.18.

$$r = \sqrt[3]{\frac{3V}{4\pi}}. \qquad (18)$$

Actual observation of dispersed particle found that volumetric errors obey a normal distribution. Therefore, we defined the radial error Δr as Eq.19.

$$\Delta r = r\cdot N(0, r_{err}/3), \qquad (19)$$

where N is a normal random number. e_{err} was set to 5% based on actual observation. The volume including the error V' is obtained by Eq.20.

$$V' = \frac{4}{3}(r+\Delta r)^3. \qquad (20)$$

The dispersed particles were regard as disappeared when they got out of the imaging range due to deformation. The total number of dispersed particles at each load step is shown in Table.II.

TABLE I
3 PARAMETER VALUES OF EACH LOAD STEP IN GLOBAL DEFORMATION

load step	*a*	*b*	*c*
5%	-0.0241	0	Inf
10%	-0.0241	0	Inf
15%	-0.04155	0	1000
20%	-0.0575	0	700
23%	-0.12	0	400

TABLE II
TOTAL NUMBER OF DISPERSED PARTICLE AT EACH LOAD STEP

load step	total number of dispersed particles
0%	20000
5%	19074
10%	18163
15%	17201
20%	16338
23%	15433

TABLE III
TOTAL NUMBERS OF LANDMARKS

landmark threshold	40000 voxels	35000 voxels	30000 voxels	25000 voxels
0%	33	54	88	109
5%	33	49	86	108
10%	33	49	82	107
15%	32	48	78	101
20%	32	47	76	103
23%	30	46	72	99

TABLE IV
TOTAL NUMBERS OF MATCHING CANDIDATES OF LANDMARKS

landmark threshold	40000 voxels	35000 voxels	30000 voxels	25000 voxels
0%	67	101	115	172
5%	67	95	123	181
10%	64	93	123	170
15%	63	89	114	165
20%	64	87	116	165
23%	61	78	106	156

B. Matching experiments and results

In our study, four landmark thresholds were given as 40,000, 35,000, 30,000 and 25,000 voxels. Table.III shows the total numbers of landmarks which were selected from a model before deformation. The numbers depends on a landmark threshold and the load step of the model before deformation. On the other hand, the dispersed particles larger than $V_{\mathrm{th}}(1-\mathrm{RC})$ voxels were selected as the matching candidates of landmarks from the model after deformation. As explained in II-A1, RC is the allowable volume change. It is highly probable that the total number of candidates is more than that of landmarks due to the lower threshold. Total candidate numbers are shown in Table.IV.

The parameters used in our method were set as shown in Table.V. As described in Section IV, ten iterations of non-landmark estimation at each landmark threshold were conducted while 80% of the landmarks was randomly selected. The best matching result was adopted by evaluating the sum of average ratios of expansion and contraction.

Matching experiments were conducted with four selecting combinations of the model before and after deformation:

(a) The model before deformation was fixed as load step 0%. The model after deformation was the other load step.
(b) The model before and after deformation of (a) were counterchanged.
(c) The model before and after deformation were adjacent load steps.

TABLE V
PARAMETERS USED IN OUR METHOD

Allowable volume change (RC)	20%
Worst ratio of expansion and contraction (W)	1
Total number of PSO particles	5
Search count of PSO	5
Random landmark sampling rate	0.8
Random landmark sampling count	10

(d) The model before and after deformation of (c) were counterchanged

(a) and (b) confirm the reliability of our matching approach. Meanwhile, (c) and (d) are assumed for actual matching.

Matching results were evaluated by two indexes: precision and recall. They are calculated by Eq.21.

$$\mathrm{precision} = R/N,\ \mathrm{recall} = R/C, \tag{21}$$

where C, N and R are the total number of the dispersed particles which should be matched, which was matched and which was correctly matched, respectively. In our study, precision is more important than recall because there are more than enough dispersed particles to evaluate D/F characteristic and fewer mismatching is preferable.

Tables VI show the matching results. In Table (a), the matching rates decrease with increasing the strain rate. Landmark disappearance before deformation negatively affected the relaxation method. Landmarks should be limited by their position so that they exist in both the model before and after deformation.

Compared with the other combinations, larger landmark thresholds tended to be select for the best matching result. To examine this result, the matching result of each volume threshold at 0%-15% is shown in Table.VII. In this matching, all landmarks were used for non-landmark estimation. As a result, landmark precision was approximately equal. However, it is easier to reject mismatching from fewer landmarks by random sampling. Therefore, larger landmark thresholds tended to be adopted.

At 0%-20%, although all landmarks were correctly matched, mismatching occurred in the overall results. Fewer landmarks were insufficient to estimate non-landmark displacement vectors in large deformation.

The result of (b) is better than that of (a). It was found that the relaxation method is resistant to noises which occurred in the model after deformation.

As shown in (c) and (d), overall precision was achieved more than 99% at every matching. The results are enough to evaluate D/F characteristics of a material.

VI. CONCLUSION

To evaluate internal thorough material characteristics in deformation, we propose the analysis method which obtains

TABLE VI
MATCHING RESULTS

(a) Results of when the model before deformation was fixed as 0%

	Selected V_{th}	Landmark		Overall		k of RBF (10^k)	Min E
		precision	recall	precision	recall		
0%-5%	25000	100% 91/91	100% 91/91	99.99% 19072/19074	99.99% 19072/19074	-5.38	470.8
0%-10%	30000	100% 69/69	100% 69/69	99.65% 17707/17770	97.49% 17707/18163	-6.25	963.8
0%-15%	40000	96% 27/28	96% 27/28	96.29% 15535/16133	90.31% 15535/17201	-5.68	2016.4
0%-20%	40000	100% 30/30	100% 30/30	95.67% 14399/15050	88.13% 14399/16338	-6.44	2558.9
0%-23%	25000	89% 55/62	92% 55/60	76.31% 7955/10425	51.55% 7955/15433	-3.21	5127.6

(b) Results of when the model before and after deformation of (a) were counterchanged

	Selected V_{th}	Landmark		Overall		k of RBF (10^k)	Min E
		precision	recall	precision	recall		
5%-0%	25000	100% 89/89	100% 89/89	100.00% 19074/19074	100.00% 19074/19074	-6.25	443.57
10%-0%	25000	100% 90/90	100% 90/90	99.71% 17694/17745	97.42% 17694/18163	-5.14	860.3
15%-0%	25000	100% 80/80	100% 80/80	98.84% 16126/16316	93.75% 16126/17201	-6.31	1346.35
20%-0%	30000	100% 63/63	100% 63/63	97.74% 14686/15026	89.89% 14686/16338	-5.67	1830.5
23%-0%	25000	99% 85/86	99% 85/86	95.56% 13070/13677	84.69% 13070/15433	-4.07	2459.9

(c) Result between adjacent load steps

	Selected V_{th}	Landmark		Overall		k of RBF (10^k)	Min E
		precision	recall	precision	recall		
0%-5%	25000	100% 91/91	100% 91/91	99.99% 19072/19074	99.99% 19072/19074	-5.38	470.8
5%-10%	30000	100% 71/71	100% 71/71	100.00% 18161/18161	99.99% 18161/18163	-6.15	454.9
10%-15%	25000	100% 80/80	100% 80/80	100.00% 17201/17201	100.00% 17201/17201	-5.82	447.7
15%-20%	25000	100% 85/85	100% 85/85	99.99% 16333/16335	99.97% 16333/16338	-3.76	472.2
20%-23%	25000	100% 80/80	100% 80/80	99.69% 15339/15387	99.39% 15339/15433	-3.89	569.7

(d) Result of when the model before and after deformation of (c) were counterchanged

	Selected V_{th}	Landmark		Overall		k of RBF (10^k)	Min E
		precision	recall	precision	recall		
5%-0%	25000	100% 89/89	100% 89/89	100.00% 19074/19074	100.00% 19074/19074	-6.25	443.57
10%-5%	25000	100% 87/87	100% 87/87	100.00% 18163/18163	100.00% 18163/18163	-5.38	429.7
15%-10%	30000	100% 62/62	100% 62/62	99.99% 17198/17199	99.98% 17198/17201	-6.32	418.5
20%-15%	25000	100% 81/81	100% 81/81	99.99% 16335/16336	99.98% 16335/16338	-3.66	444.1
23%-20%	25000	100% 82/82	100% 82/82	99.86% 15385/15406	99.69% 15385/15433	-3.25	512.6

displacement vectors of dispersed particles between deformation from nano-order 3D-CT images. In this paper, we improved our matching approach. To achieve more robust matching and eliminate the need to determine the best landmark threshold, our method prepared a number of landmark thresholds. Then, each matching was performed in parallel. Non-landmark estimation was iterated while a percentage of the landmarks was randomly selected. k of a RBF was optimally-estimated by PSO. To reduce mismatching, overlap matching was deleted. Overall precision was achieved more than 99% at every matching between adjacent load steps.

In further work, mismatching except overlap matching will be dealt. As the final goal of the study, some experiments under various real tests will be conducted.

TABLE VII
RESULT OF MATCHING LOAD STEP 0%-15%

V_{th}	Landmark		Overall		E
	precision	recall	precision	recall	
25000	96% 94/98	97% 94/97	95.30% 14769/15497	85.86% 14769/17201	2418.5
30000	95% 79/83	98% 79/81	92.05% 14296/15531	83.11% 14296/17201	2792.2
35000	92% 49/53	98% 49/50	86.76% 13142/15148	76.40% 13142/17201	3423.3
40000	94% 31/33	97% 31/32	94.18% 15150/16087	88.08% 15150/17201	2290.6

all landmarks were used for non-landmark estimation

REFERENCES

[1] L. Allais, M. Bornert, T. Bretheau and D. Caldemaison, Experimental characterization of the local strain field in a heterogeneous elastoplastic material, Acta Metall Mater, Vol.42, pp.3865-3880, 1994

[2] Y. L. Liu and G. Fischer, In situ measurement of local strain in a metal matrix composite by the object grating technique, Scr Mater, Vol.36, pp.1187-1194, 1997

[3] N. Deng and I. Yamaguchi, Automatic analysis of speckle photographs with extended range and improved accuracy, Appl Opt, Vol.29, pp.296-303, 1990

[4] L. Larsson, M. Sjodahl, F. Thuvander, Microscopic 3-D displacement field measurements using digital speckle photography, Opt Lasers Eng, Vol.41, pp.767-777, 2004

[5] R. Shabadi, S. Kumar, H. J. Roven, E. S. Dwarakadasa, Characterisation of PLC band parameters using laser speckle technique, Materials Science and Engineering, Vol.364, pp.140-150, 2004

[6] Daniel Post, Moire interferometry: Advances and applications, Experimental Mechanics, Vol.31, pp.276-280, 1991

[7] Colin A. Walker, A historical review of Moire interferometry, Experimental Mechanics, Vol.34, pp.281-299, 1994

[8] G. Nicoletto, On the visualization of heterogeneous plastic strains by Moire interferometry, Opt Lasers Eng, Vol.37, pp.433-442, 2002

[9] L. Qian, H. Toda, K. Uesugi, T. Kobayashi, T. Ohgaki, and M. Kobayashi, Application of synchrotron x-ray microtomography to investigate ductile fracture in Al alloys, Applied Physics Letters, Vol.87, 241907, 2005

[10] S.F. Nielsen, H.F. Poulsen, F.Beckmann, C.Thorning and J.A. Wert, Measurements of plastic displacement gradient components in three dimensions using marker particles and synchrotron X-ray absorption microtomography, Acta Mater, Vol.51, pp.2407-2415, 2003

[11] M. Nakazawa et al., A Proposal of a Method to Analyze 3D Deformation / Fracture Characteristics inside Materials Based on a Stratified Matching Approach, Proc. of IECON2009, Porto, 2009, *accepted*

[12] A. Rosenfeld, R.A. Hummel, and S.W. Zucker, Scene Labeling by Relaxation Operation, IEEE Trans. Systems, Man, and Cybernetics, Vol.6, pp.420-433, 1976

[13] F. Pighin, J. Hecker, D. Lichinski et al, Synthesizing Realistic Facial Expressions from Photographs, Proc SIGGRAPH98, pp.75-84, 1998

[14] K. Okamoto, Y. A. Hassan and W. D. Schmit, New Tracking Algorithm for Particle Image Velocimetry, Experiments in Fluids, Vol.19, pp.342-347, 1995

[15] J. Kennedy and R. Eberhart, Particle Swarm Optimization, Proc. of IEEE International Conference on In Neural Networks, Vol.4, pp.1942-1948, 1995

[16] F. Scarano, Iterative image deformation methods in PIV, Meas. Sci. Technol. Vol.13, pp. R1–R19, 2002

[17] Willert, C. E. and Gharib, M., Digital particle image velocimetry, Fluid Measurement and Instrumentation Forum, ASMEFED-Vol.95, pp.39-44, 1990
[18] K. Ohmi, N. Yoshida and H. T. Hoang, Further Improvement of Genetic Algorithm PTV, Journal of the Visualization Society of Japan, No.2, Vol.21, pp.35-38, 2001, *in Japanese*
[19] K. Ohmi and N. Yoshida, Neural network PTV using a self-organizing maps method, Journal of the Visualization Society of Japan, No.1, Vol.21, pp.125-128, 2001, *in Japanese*
[20] K. Yamamoto, Recognition of Handprinted KANJI Characters by Relaxation Matching, IEICE Trans. Inf. & Syst., Vol.J65-D, No.9, pp.1167-1174, 1982, *in Japanese*
[21] Y. Kanehira et al., Relaxed Multiple Template Matching for Estimating Sea Surface Velocity Field, IEICE Trans. Inf. & Syst., Vol.J86-D-2, No.6, pp.846-855, 2003, *in Japanese*
[22] K. Iwata et al., Facial Parts Detection by Using Four Directional Features and Relaxation Matching, IEEJ Trans. EIS, Vol.124, No2, pp.706-712, 2004, *in Japanese*
[23] N. Oka et al., Optimization of Similarity Evaluation Algorithm Using Relevance Feedback in Content-Based Image Retrieval, Journal of Japan Society for Fuzzy Theory and Intelligent Informatics, Vol.19, No.5, pp.524-536, 2007, *in Japanese*
[24] C.B. Barber, D.P Dobki and H.T. Huhdanpaa, The Quickhull Algorithm for Convex Hulls, ACM Trans. on Mathematical Software, Vol.22, pp.469-483, 1996